Chemistry–A European Journal

Full Paper
doi.org/10.1002/chem.202102829

Chemistry Europe
European Chemical
Societies Publishing

Special Issue

Synergistic Effects of Co and Fe on the Oxygen Evolution Reaction Activity of LaCo$_x$Fe$_{1-x}$O$_3$

Achim Füngerlings+,[a] Adarsh Koul+,[b] Maik Dreyer+,[c] Anna Rabe,[c] Dulce M. Morales,[d] Wolfgang Schuhmann,[b] Malte Behrens,[c, e] and Rossitza Pentcheva*[a]

Abstract: In a combined experimental and theoretical study we assess the role of Co incorporation on the OER activity of LaCo$_x$Fe$_{1-x}$O$_3$. Phase pure perovskites were synthesized up to $x = 0.300$ in 0.025/0.050 steps. HAADF STEM and EDX analysis points towards FeO$_2$-terminated (001)-facets in LaFeO$_3$, in accordance with the stability diagram obtained from density functional theory calculations with a Hubbard U term (DFT+U). Linear sweep voltammetry conducted in a rotating disk electrode setup shows a reduction of the OER overpotential and a nonmonotonic trend with x, with double layer capacitance measurements indicating an intrinsic nature of activity. This is supported by DFT+U results that show reduced overpotentials for both Fe and Co reaction sites with the latter reaching values of 0.32–0.40 V, ~0.3 V lower than for Fe. This correlates with a stronger reduction of the binding energy difference of the *O and *OH intermediates towards an optimum value of 1.6 eV for $x = 0.250$, the OH deprotonation being the potential limiting step in most cases. Significant variations of the magnetic moments of both surface and subsurface Co and Fe during OER demonstrate that the beneficial effect is a result of a concerted action involving many surrounding ions, which extends the concept of the active site.

1. Introduction

The development and commercialization of water electrolysis technologies for the sustainable production of hydrogen face currently a need for high-performance catalysts based on earth-abundant elements that are able to drive the oxygen evolution reaction (OER) at low overpotentials. Transition metal oxide-based catalysts have been extensively studied and have shown promising OER activity in alkaline media.[1–4] Besides low cost and high abundance, their ability to obtain various oxidation states and adapt to different coordination environments represent some of the key ingredients enabling tunable electrocatalytic performance. Lately, it has been observed that a combination of different transition metal cations may be beneficial to reduce the overpotentials for oxidation processes.[5–7] These effects have been attributed to the tuning of adsorption energy differences,[8] consequently affecting the potential-limiting step, as well as to differences in electrical conductivity.[9] Notably, the combination of Fe and Co has shown evidence for improved electrochemical activity in metal oxides,[10–13] in particular in Co and Fe containing spinels,[7,14–18] phosphides,[10,19] borides and nitrides.[20–24]

Perovskites (chemical formula ABO$_3$) represent another interesting class of metal oxides that allows for broad tuning of properties through variation of the A- and B-cations.[25] Several reviews address their activity for the oxygen evolution reaction.[1,26,27] Individual and combined A- and B-site mixing, as e.g. in (Ba,Sr)Co$_x$Fe$_{1-x}$(BSFO) or La$_x$Sr$_{1-x}$CoO$_3$ has emerged as a promising strategy for optimizing anode materials for OER.[5,28] Here the e_g orbital occupation was identified as a descriptor of OER activity,[29] where the improved performance of BSCFO was ascribed to an optimum occupation of the e_g orbitals of 1.2

---

[a] A. Füngerlings,+ R. Pentcheva
Department of Physics,
Theoretical Physics and Center of Nanointegration (CENIDE),
University of Duisburg-Essen,
47057 Duisburg, Germany
E-mail: rossitza.pentcheva@uni-due.de

[b] A. Koul,+ W. Schuhmann
Analytical Chemistry-Center for Electrochemical Sciences (CES),
Faculty of Chemistry and Biochemistry,
Ruhr University Bochum,
44780 Bochum, Germany

[c] M. Dreyer,+ A. Rabe, M. Behrens
Faculty for Chemistry,
Inorganic Chemistry and Center of Nanointegration (CENIDE),
University of Duisburg-Essen,
45141 Essen, Germany

[d] D. M. Morales
Nachwuchsgruppe Gestaltung des Sauerstoffentwicklungsmechanismus,
Helmholtz-Zentrum Berlin für Materialien und Energie GmbH,
Hahn-Meitner-Platz 1, 14109 Berlin, Germany

[e] M. Behrens
Institute for Inorganic Chemistry,
Christian-Albrechts-Universität zu Kiel,
24118 Kiel, Germany

[+] Contributed equally

Supporting information for this article is available on the WWW under https://doi.org/10.1002/chem.202102829

Part of a Special Issue on Contemporary Challenges in Catalysis.

which tunes the B–O binding energy.[26] Furthermore, the critical role of the Co 3*d* – O 2*p* covalency as a function of Sr substitution at the A site,[26,30,31] the role of oxygen vacancies and the stabilization of higher spin states of Co in nanoparticles have been recognized.[26,30,32–34] Previous theoretical studies on LaXO$_3$ suggest that LaCoO$_3$ has a higher OER activity than LaFeO$_3$.[32,35–38] Here, we focus particularly on the effect of cation mixing at the B-site and present a combined theoretical and experimental study of the LaFeO$_3$-LaCoO$_3$ series as an OER catalyst to gain insight into possible synergy effects between Co and Fe.

LaCo$_x$Fe$_{1-x}$O$_3$ (LCFO) has previously been synthesized and studied as a catalyst for various reactions involving hydrocarbons.[39–41] The synthesis of LCFO by thermal decomposition of amorphous precursor materials by constant pH co-precipitation was recently reported.[42] While previous studies have concentrated on the Co-rich limit,[34] here we concentrate on the Fe-rich phases with samples synthesized in small steps of 0.025 to 0.050 in the range up to $x = 0.300$ to avoid the formation of secondary phases. Rotating disk electrode voltammetry is applied to study the OER activity with Co substitution. The nature of the observed effects is probed by double layer capacitance experiments. To investigate the role of Co incorporation on the OER overpotential and the origin of the non-monotonic trend and shed light on the underlying mechanisms, we have performed density functional theory calculations with a Hubbard U term. Prior to assessing the OER activity, we discuss the properties of bulk LCFO and identify the relevant surface orientations and terminations in the framework of *ab initio* thermodynamics. Moreover, the coverage of the surface with O- and OH-groups under reaction conditions as a function of applied voltage and pH is compiled in a Pourbaix diagram. The calculated OER overpotentials are compared to the experimental data and correlated to the binding energy difference of *O and *OH. To gain further understanding, the energetic trends are traced back to the changes in electronic properties in terms of variation of the oxidation state of the reaction site and its neighbors during OER.

2. Results and Discussion

2.1. Catalyst Synthesis and Characterization

LaCo$_x$Fe$_{1-x}$O$_3$ perovskites were obtained through thermal decomposition of amorphous precursor materials synthesized by constant pH co-precipitation in a semi-automatized lab reactor system as reported previously.[42] The materials in this study were freshly synthesized in steps of 0.025 to 0.050 difference in Co content determined by the Co/(Co + Fe) ratio, in order to study the effect of composition differences on the catalytic properties in small steps.

Powder X-ray diffraction (XRD) patterns of the co-precipitated precursors are shown in the Supporting Information in Figure S1. For $x > 0.050$, the formation of a crystalline secondary phase corresponding to the (003) reflection of the CoFe-hydrotalcite (ICSD collection code 6296) was observed at 12° 2θ,[43] as reported before,[42] which increased with the nominal Co content in the metal salt solution used in synthesis. The precursor materials were slightly Co deficient compared to Fe, as was observed in the experimentally determined Co/(Co + Fe) ratio (x_{exp}) from atomic absorption spectroscopy (AAS), as shown in Table S1. The deficiency in Co matched well with the lattice parameters after Rietveld refinement of the perovskite catalysts derived after thermal decomposition and is slightly less pronounced compared to the previous report.[42]

In Figure 1(a), the XRD patterns of the materials after thermal treatment at 800 °C are shown. Sample $x = 0.000$ corresponds to orthorhombic LaFeO$_3$ (ICSD: 93611).[44] With increasing Co content, the reflections were shifted to higher angles (indicated by the dotted line at the most intensive (112) reflection, see also zoom-in of this peak in Figure 1(b)) showing that the incorporation of Co into the orthorhombic perovskite structure is accompanied by a decrease in the lattice spacings due to the smaller effective ionic radius of low-spin Co^{3+} in comparison to Fe^{3+} in octahedrally coordinated sites.[45,46] The reduction of the lattice parameters with x is supported also by the DFT + U calculation, a comparison is shown in Figure 3. From our previous work, also a distortion of the M-O$_6$ octahedra is expected, that results in a weaker force constant of the transition metal oxygen bond.[42,47]

From transmission electron microscopy (TEM), faceted crystalline particles were detected, as also reported in a previous study.[42] An exemplary image for $x = 0.000$ is shown in Figure 1(c). The high-angle annular darkfield (HAADF) scanning TEM (STEM) image in Figure 1(d) with a viewing direction along the [110] direction and an overlay of the crystal structure indicates a (001) termination of the particle at the upper right row of the image indicated by a red arrow. From energy-dispersive X-ray spectroscopy (EDX) elemental mapping, the A and B cation layers can be identified and the image suggests a B-termination of this LaFeO$_3$ particle, as shown in Figure 1(e). The pattern of the Fe and La ions follow the contrast changes in the right side of the image in the not-mapped area.

Adsorption isotherms for the calcined perovskite samples are displayed in Figure S2(a), N$_2$ in the Supporting Information. All isotherms were described by a type IVa hysteresis loop.[48] The corresponding pore-size distributions are shown in Figure S2(b). The distributions were derived via the BJH method from desorption data. The pore size distributions showed a maximum in the range of 20–30 nm for the samples, indicating mainly interparticle pores. In Table S1, BET surface areas calculated from p/p_0 data between 0.05 and 0.3, average pore sizes determined by the BJH method during desorption and total pore volumes determined at $p/p_0 = 0.99$ are listed. None of them showed a clear trend with Co content. The pore volumes seemed to be increasing up to $x = 0.100$, but decreased again beyond this value. The same applied to the BET surface area, with an outlier at $x = 0.250$. Overall, there is no clear correlation between the adsorption-desorption behavior and the Co content.

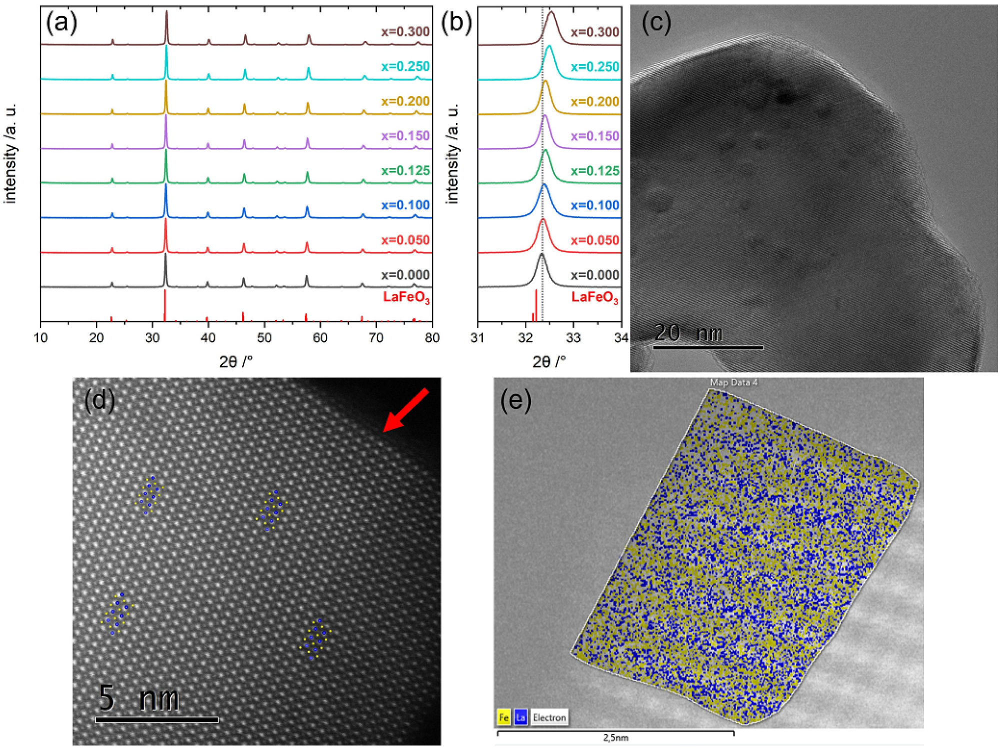

Figure 1. (a) XRD powder patterns of the calcined materials. (b) XRD powder patterns of the (112) reflections. (c) HR-TEM micrograph of $x = 0.000$. (d) HAADF STEM micrograph of $x = 0.000$ with insets of the $LaFeO_3$ lattice along the [110] direction, lanthanum ions are shown in blue, iron ions in yellow. (e) STEM elemental mapping in a selected area showing the A and B cation layers, oriented along the (001)-direction, lanthanum ions are shown in blue, iron ions in yellow.

2.2. Catalytic Activity Measurements

Investigation of the OER activity of the different perovskite samples was conducted by rotating disk electrode voltammetry. The averages of three independent measurements are shown in Figure 2(a). Evidently, the sample with the lowest activity in terms of overpotential and current density was $LaFeO_3$. A substantial decrease in the OER overpotentials is observed even with a minor addition of Co to the perovskite structure. In order to evaluate the OER activity in relation to the cobalt content, the potentials required to reach a current density of 10 mA/cm^2, $E_{J=10}$, were extracted from the voltammograms shown in Figure 2(a) as a function of the composition with increasing cobalt content x, Figure 2(b). The obtained values are summarized in Table S2. Since the data show no clear correlation between measured overpotentials and BET, the effect of BET surface area on the electrochemical reaction can be neglected, whereas the Co content is decisive. For the pristine Fe perovskite, i.e., $LaFeO_3$, $E_{J=10}$ was 1.760 V. For the samples with $x = 0.05, 0.10$, $E_{J=10}$ values of 1.702 and 1.682 V were obtained, which are lower by about 60 and 80 mV than that of $LaFeO_3$, respectively. Similar trends of increased activity upon incorporation of small amounts of Co into a Fe oxide structure have been observed previously.[49,50] However, further Co incorporation led to an overall increase in overpotentials, rendering $LaCo_{0.1}Fe_{0.9}O_3$ ($x = 0.100$) the perovskite with the lowest overpotential (1.682 V) among the investigated catalysts.

It may be speculated that the observed increase in the OER overpotentials at $x > 0.100$ could be caused by a decrease in electrical conductivity due to a lower Fe content, since it has been reported that Fe has a favorable impact on the electrical conductivity.[9,51] Assuming that the differences in electrical conductivities become more evident at larger electrode potentials according to Ohm's law, the current densities measured at a potential of 1.8 V vs RHE ($J_{1.8}$) were extracted from the voltammograms shown in Figure 2(a) and compared as a function of the Co content, Figure 2(c). The obtained values are summarized in Table S2. The cobalt-free perovskite exhibited the lowest current of $J_{1.8} \approx 19\ \mathrm{mA/cm^2}$, whereas $LaCo_{0.1}Fe_{0.9}O_3$ displayed the largest current density, with $J_{1.8} \approx 45\ \mathrm{mA/cm^2}$. Further increase in Co content led to lower current densities. Even though similar activity trends were displayed with the activity parameters $E_{J=10}$ and $J_{1.8}$, for the latter a more pronounced nonmonotonic trend was observed at larger Co contents. Thereby, differences in electrical conductivity alone cannot explain the observed activity trend in relation to the composition.

Differences in the electrochemically active surface area (ECSA) may also play a role in the observed activity trend. To investigate this, double layer capacitance, C_{DL}, which is proportional to the ECSA, was determined for the different samples by scan rate-dependent cyclic voltammetry following a procedure reported recently.[52] An example of collected CVs and the resulting charging current vs scan rate plot is shown in the

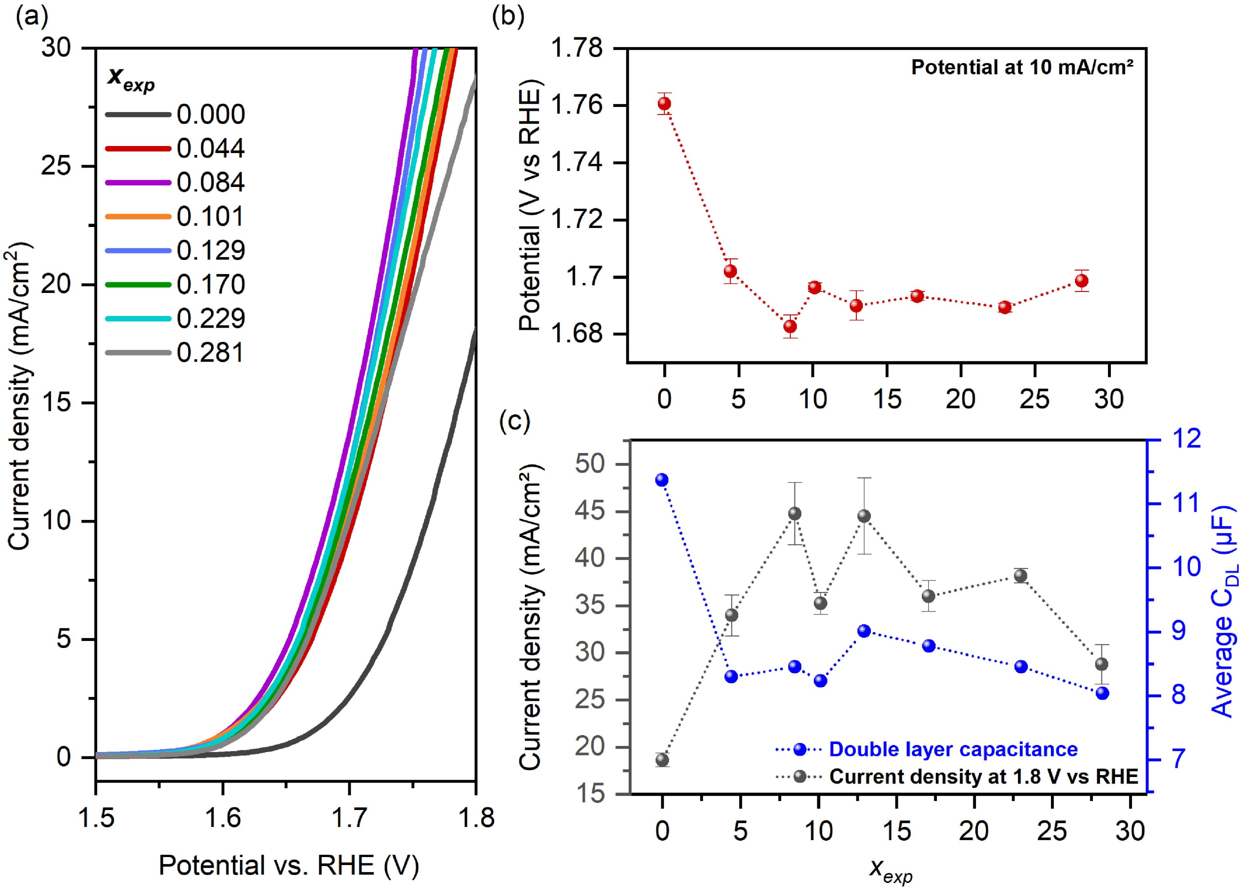

Figure 2. (a) Linear sweep voltammograms of $LaCo_xFe_{1-x}O_3$ perovskites recorded at a scan rate of 5 mV/s and electrode rotation of 1600 rpm in Ar-saturated 1 M KOH as electrolyte, and the corresponding (b) potentials measured at 10 mA/cm², and (c) current densities attained at 1.8 V vs. RHE and average double layer capacitance (C_{DL}). Error bars in (b) and (c) represent the standard deviation.

Supporting Information (Figure S3). The average C_{DL} values obtained for each of the samples using the allometric regression model are reported in Table S3 along with their respective coefficient of determination, R^2, and exponent, α, and are additionally shown in Figure 2(c). The C_{DL} values exhibited by the different perovskite samples were rather similar, ranging from 8 to 11 μF. However, the C_{DL} plot also follows a nonmonotonic trend in the x range between 0.05 and 0.2, which could explain the nonmonotonic pattern seen for the activity parameters $E_{J=10}$ and $J_{1.8}$, in this same cobalt content range. Yet, the highest capacitance (~11 μF) was obtained with the sample $x=0$, which was also the perovskite that exhibited the lowest OER currents and largest overpotentials, indicating that the observed differences in activities are not only due to differences in ECSA or electrical conductivity, as discussed earlier, but also to differences in intrinsic activity.

2.3. DFT+U calculations

In order to explore the origin of improved OER activity of $LaCo_xFe_{1-x}O_3$ with Co incorporation and the nonmonotonic dependence on concentration, we performed density functional theory calculations with a Hubbard U term. The OER performance of $La\,Co_x\,Fe_{1-x}\,O_3$ was investigated for four different Co concentrations: with $x=\{0, 0.125, 0.250, 0.500\}$. In a first step, we assessed the bulk properties of $LaCo_xFe_{1-x}O_3$ for these concentrations. Transition metal cations, in particular Co, can exist in different spin states: high (HS), intermediate (IS) or low spin (LS) state.[53–56] Moreover, the B cations' spins can order either ferro- or antiferromagnetically. Furthermore, different arrangements of the Co and Fe-cations are possible. All possible B-cation arrangements within a 2 × 2 × 2 unit cell in combination with possible magnetic configurations as well as high and low spin states were examined and the relative stability of these configurations as a function of x are listed in Table S6 in the SI. The lowest energy configuration across all concentrations turned out to be Co having only Fe nearest neighbors (G-type cation order), with all Co-ions being Co^{3+} LS with nearly quenched magnetic moment (0.11–0.28 μ_B) and all Fe-ions in Fe^{3+} HS with a magnetic moment of $\sim 4.1\,\mu_B$ and G-type antiferromagnetic (G-AF) order (i.e. nearest Fe-neighbors with opposite spin). Only for $x=0.500$ the latter competes with a ferromagnetic configuration. Furthermore, for $x=0.250$ we observed a close competition between the different cation orders, but most importantly also the Co HS configuration lies close in energy. A similar effect was reported previously for the Co-rich limit ($x = 0.900$).[34] The spin densities of the most stable configurations for each concentration are shown in Figure 3(a). The measured and calculated lattice parameters are displayed in Figure 3(b) and exhibit a decrease as a function of cobalt concentration, albeit the theoretical values are slightly lower, which is likely related to the choice of the PBEsol exchange correlation functional. Moreover, we determined the B–O–B bond angles as a measure of the lattice distortion and octahedral tilts and rotations (the stronger the deviation from 180°, the stronger the distortion). While in LFO the calculated Fe–O–Fe angles are $\sim 155^\circ$, they are slightly lowered to $\sim 154^\circ$ for $x = 0.125$ and subsequently increase to $\sim 156^\circ$ for $x = 0.250$. Likewise, also the Co–O–Fe angles show a non-monotonic trend varying from $\sim 158^\circ$ for $x = 0.125$ to $\sim 156^\circ$ for $x = 0.250$ and $\sim 161^\circ$ for $x = 0.500$.

For an initial assessment of changes of bulk conductivity due to Co mixing in LCFO, we report the DFT+U projected density of states and band gaps for the studied concentrations (see Figure S5 in SI). The band gaps are substantially reduced from 2.15 eV for $LaFeO_3$ to 1.68 eV ($x = 0.125$), 1.64 ($x = 0.250$, here the Co HS state has a lower gap of 1.07 eV due to a localized state in the gap) and 1.47 eV ($x = 0.500$, here the FM configuration has a similar band gap of 1.42 eV).

In order to select the most relevant surface orientations and terminations for the OER modelling, we determine their stability in the framework of *ab initio* thermodynamics,[57,58] using Eq. (5), as described in the Methods Section. The surface phase diagram was constructed for the (001), (110) and (111) orientations with two possible terminations each.

Figure 4 displays the most stable favorable orientations and terminations as a function of the chemical potentials of La and O. The relevant synthesis conditions coincide with a region of

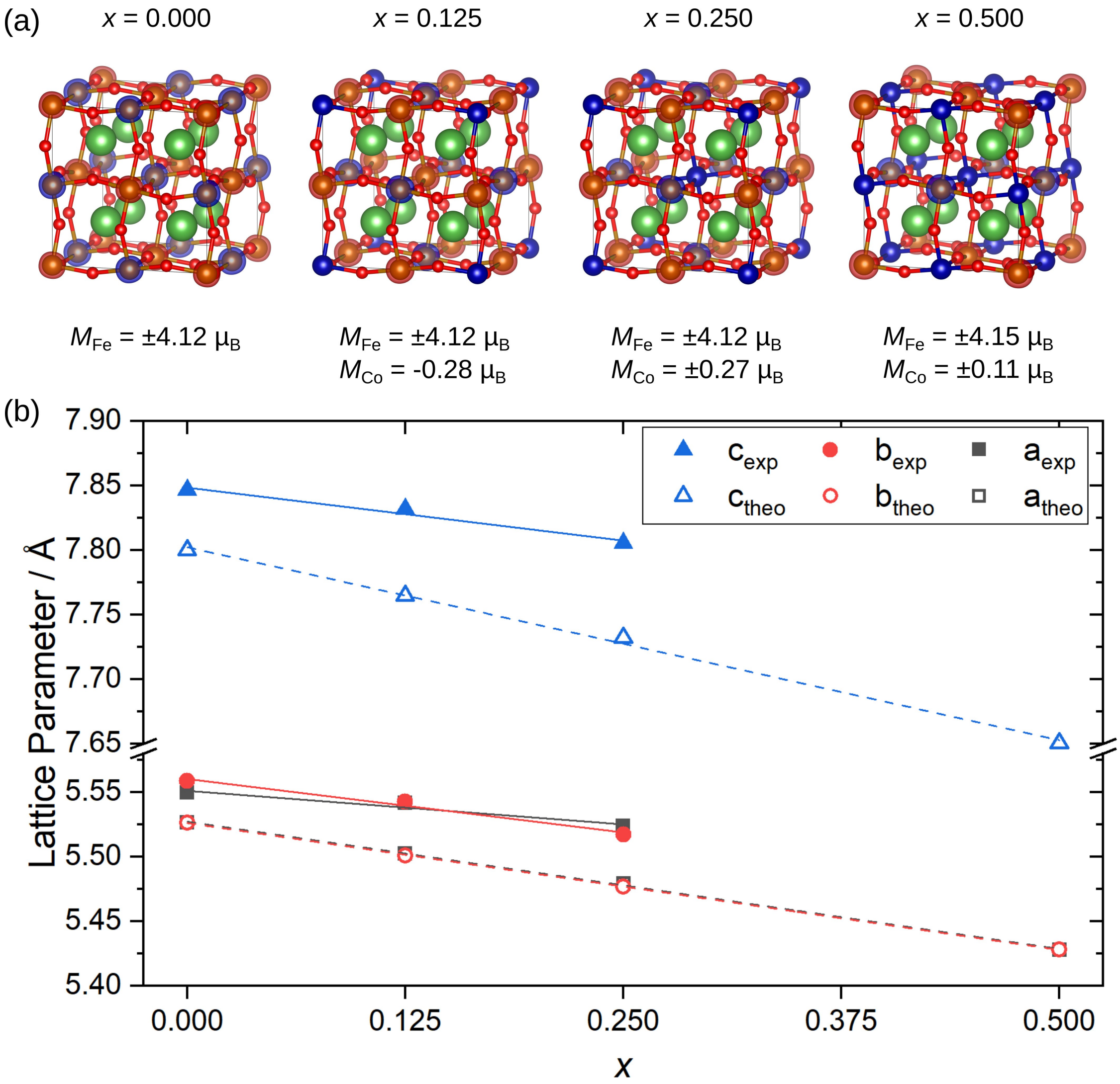

Figure 3. (a) Relaxed structures of the most stable configurations of bulk $LaCo_xFe_{1-x}O_3$ (G-type cation and antiferromagnetic order with Fe (HS) and Co (LS)) together with the spin-densities for the different Co concentrations. Green, bronze, blue and red spheres denote La, Fe, Co and O, respectively. Red and blue clouds indicate positive and negative spin densities in the antiferromagnetically coupled systems. Additionally, the magnetic moments of Fe and Co are given. (b) Comparison of experimental and theoretical lattice constants as a function of Co/(Co+Fe) ratio.

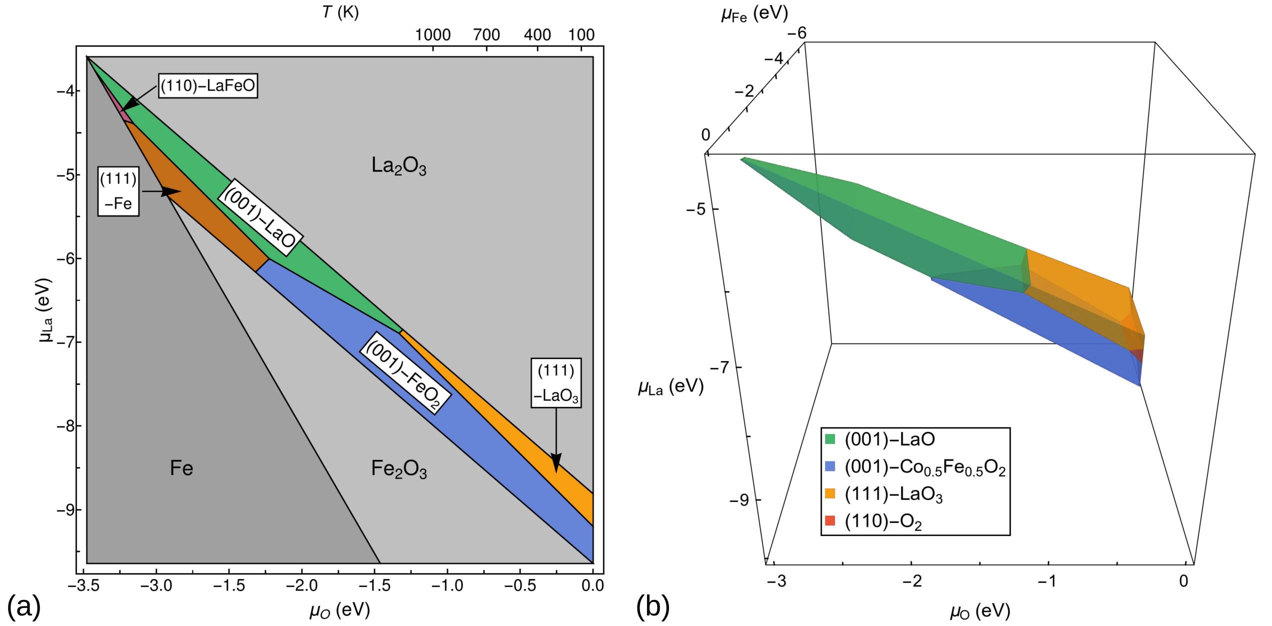

Figure 4. Surface stability diagrams for (a) $LaFeO_3$ and (b) $LaCo_{0.5}Fe_{0.5}O_3$ showing the most stable orientations and terminations as a function of μ_{La} and $\mu_O(T, p_{O_2})$. On the top axis the latter is converted into T for $p_{O_2} = 1$ atm.

stability of the BO_2-termination of the (001) surface. This is also consistent with the (001) orientation and the Fe enrichment at the surface obtained from TEM (cf. Figure 1(e)). Therefore in the following we focus on the BO_2(001) termination to study the OER activity.

When the catalyst's surface is in contact with an aqueous solution, oxo- and hydroxyl-groups are expected to form, the extent and composition depending on the solution's pH as well as on the applied voltage. A surface Pourbaix diagram was constructed to explore the stability of surface functional groups using Eq. (6), as described in the Computational Section, see also Ref. [59]. The four B-cation sites at the surface were covered by one to four $^*O$ and/or $^*OH$ corresponding to one quarter to a full monolayer (ML) in all possible combinations regarding also the order of cations at the B-sites. From all studied combinations the system with the lowest free energy was selected. The Pourbaix diagrams for $LaFeO_3$(001) and $LaCo_{0.5}Fe_{0.5}O_3$(001) in Figure 5 show a broad region of stability of the clean surface up to 1.7 V and 1.5 V for the former and latter, respectively, followed by an increasing coverage by hydroxyl groups and subsequently mixed and oxygenated surfaces with increasing voltage. The calculated OER potentials, ϕ_{OER}, derived from Eq. (12), are also shown in Figure 5 by dashed lines. For $LaCo_{0.5}Fe_{0.5}O_3$(001), ϕ_{OER} of the precovered surfaces lies in the region of corresponding coverage, 1/4 ML OH and 1/4 ML O. For $LaFeO_3$(001), the region of stability 1 ML OH is broader and ϕ_{OER} lies slightly above the border to a mixed OH and O coverage. Since also the experimentally applied voltage (1.76 V at pH 13) lies in this region, we have investigated the OER for 1 ML OH-coverage besides the clean surface. This coverage was also adopted for $x = 0.125$ and $x = 0.250$.

Figure 6(a) shows the overpotentials η (see Eq. (14) in the Methods section) for the clean and precovered surfaces of $LaCo_xFe_{1-x}O_3$(001) with BO_2 termination as a function of Co contents for both Fe and Co reaction sites. For both reaction sites a reduction of the overpotential with x is observed compared to the end member $LaFeO_3$ ($\eta = 1.0$ V), demonstrating the favorable role of Co substitution. Overall, the overpotentials for Co reaction sites are lower than for Fe. The precovered surfaces tend to have higher overpotentials, except for a Co site at the surface covered by 1 ML OH at $x = 0.250$, where the lowest overpotential of 0.32 V is obtained. Furthermore, the trend is overall nonmonotonic, with the above mentioned minimum for a Co reaction site for the precovered surface at $x = 0.250$ and subsequent slight increase (the minimum for the uncovered surface is at $x = 0.125$). For Fe as the reaction site the overpotential decreases from initially 1.0 V ($x = 0.000$) to 0.82 V ($x = 0.125$), then increases to 0.93 V ($x = 0.250$) and subsequently decreases to 0.63 V for $x = 0.500$. The nonmonotonic trend in the calculated OER overpotentials is consistent with the experimental observation in Figure 2(b) and the presence of an outlier at $x = 0.250$.

To gain more insight, in Figure 6(b) we have plotted the overpotential as a function of the binding energy difference $G^b_O - G^b_{OH}$, the so-called volcano plot.[35] The results show that all cases lie on the strong binding leg and reflect both the nonmonotonic trend with coverage, but in particular the improvement of η with the reduction of the binding energy difference towards an optimum value below 1.6 eV,[16,18] achieved for the Co site at the fully hydroxylated surface at $x = 0.250$. Interestingly, values of η for Co and Fe sites are well separated, the latter lying at much higher binding energy differences between 2.2 and 2.4 eV.

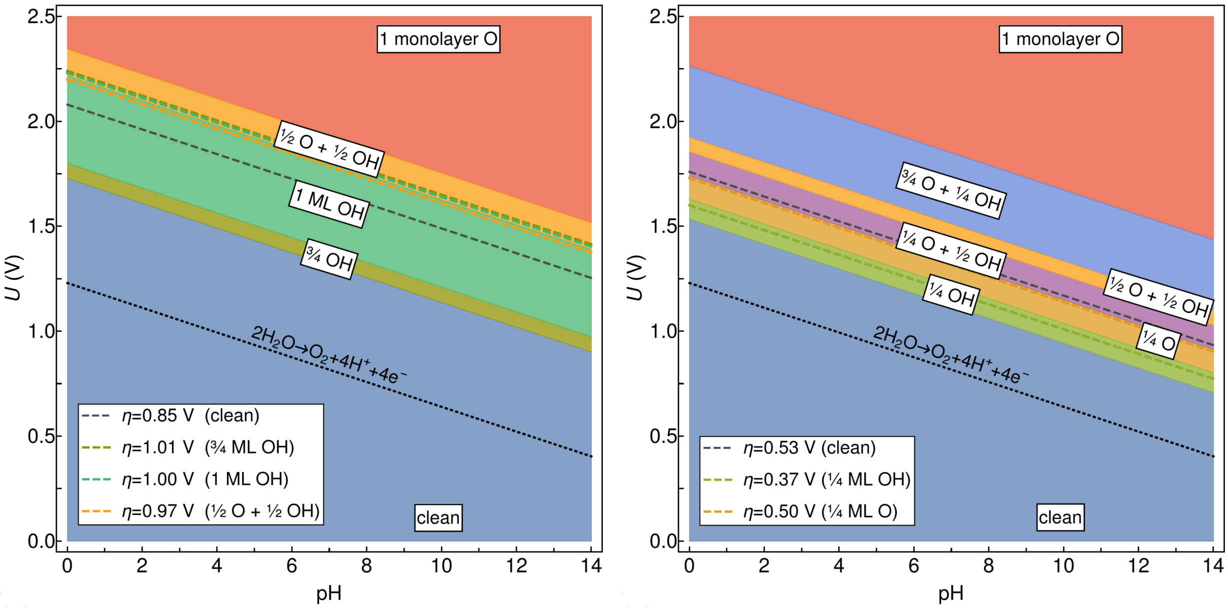

Figure 5. Pourbaix diagrams for (a) $LaFeO_3(001)$ and (b) $LaCo_{0.5}Fe_{0.5}O_3(001)$ showing the most stable coverage as a function of applied voltage and pH value. Dashed lines indicate the highest reaction free energy that determines the overpotential for OER, which can be plotted as a function of pH, according to Eq. (12), as described in the Methods section.

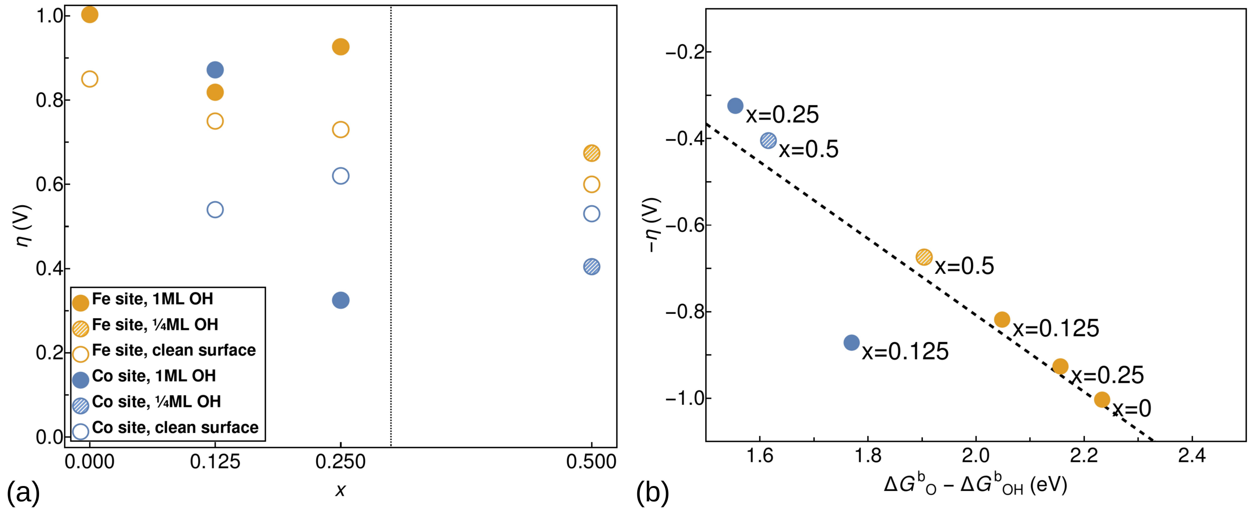

Figure 6. (a) OER overpotential as a function of Co concentration. The dashed vertical line at $x=0.3$ indicates the threshold up to which phase-pure perovskite samples could be synthesized and OER activity was measured experimentally (see Figure 2(b)). (b) Overpotential as a function of the difference of $^{*}O$ and $^{*}OH$ adsorption energies for covered surfaces with linear fit to the data with slope: 0.88 V/eV.

In order to gain further understanding of the effect of Co mixing and the nonmonotomic trend of the overpotential with x, we have plotted in Figure 7 the cumulative reaction free energies of Fe- and Co-sites for all compounds. ΔG_i and η are also listed in Table 1 (the individual steps are defined in Equations (7)—(10) in the Methods section). In most cases the potential determining step turns out to be $^{*}OH \rightarrow^{*} O$ (step 2), except for a Fe site at the clean and a Co site at the precovered surface for $x=0.125$, where ΔG_1 – the formation of *OH – is highest. Overall, the potential determining steps for Fe reaction sites are $\sim 0.2-0.3$ eV higher than for Co and increase by ~ 0.2 eV for the hydroxylated surface, resulting overall in higher overpotentials for Fe sites than for Co. For the latter, hydroxylation reduces the overpotential by 0.30 and 0.13 eV for $x=0.250$ and $x=0.500$, respectively. The Co site at the hydroxylated surface for $x=0.125$ marks the only case where the overpotential of a Co site is increased and comparable to the ones of the Fe sites. Altogether, especially for the higher concentrations of Co, the heights of the individual intermediate steps become comparable, which is a desirable feature for optimum OER activity[35] and has also been predicted for spinel surfaces, $CoFe_2O_4(001)$ and $Co_3O_4(001)$.[16,18]

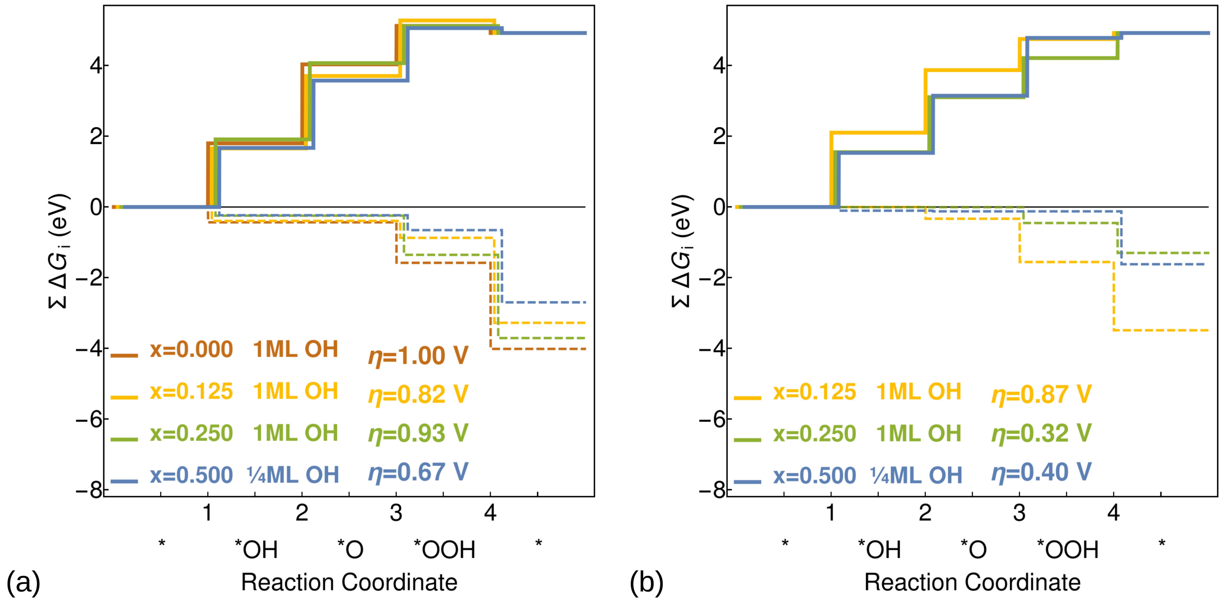

Figure 7. Cumulative reaction free energies of the OER intermediates (solid lines) for covered surfaces at (a) Fe- and (b) Co-reaction sites. The values under applied external potential ϕ are denoted by dashed lines.

Table 1. Reaction free energies of intermediates and the resulting overpotential for Fe and Co reaction sites at the clean and hydroxylated $LaCo_xFe_{1-x}O_3(001)$ surface. Potential determining steps are emphasized with bold font.

x	ΔG_1 (eV)	ΔG_2 (eV)	ΔG_3 (eV)	ΔG_4 (eV)	η (V)
Fe site (clean surface)					
0	1.80	**2.08**	1.27	-0.24	0.85
0.125	**1.97**	1.81	1.01	0.12	0.74
0.25	1.49	**1.96**	1.15	0.33	0.73
0.5	1.67	**1.83**	1.26	0.15	0.60
Fe site (hydroxylated)					
0	1.80	**2.23**	1.09	−0.20	1.00
0.125	1.66	**2.05**	1.57	−0.35	0.82
0.25	1.91	**2.16**	1.05	−0.20	0.93
0.5	1.67	**1.90**	1.48	-0.14	0.67
Co site (clean surface)					
0.125	1.11	**1.77**	1.15	0.89	0.54
0.25	1.17	**1.85**	1.43	0.47	0.62
0.5	1.53	1.63	**1.76**	-0.00	0.53
Co site (hydroxylated)					
0.125	**2.10**	1.77	0.88	0.17	0.87
0.25	**1.55**	**1.55**	1.11	0.71	0.32
0.5	1.53	**1.62**	**1.63**	0.14	0.40

We next correlate the energetic trends with the underlying electronic properties. Figures 8 and 9 show the side views of the structures, spin density and magnetic moments of cations for the OER intermediates for different Co concentrations and Fe and Co reactions sites, respectively. We start with the Fe reaction site in Figure 8: For $x=0.000$ the hydroxylated surface (except for the reaction site) prior to adsorption (*) shows bulk-like behavior with Fe^{3+} (magnetic moment $\sim 4.1\mu_B$) in the third layer and an increasing fraction of Fe^{2+} (magnetic moment $\sim 3.5-3.6\mu_B$) in the subsurface (50 %) and surface layers (75 %), with antiferromagnetic order in all layers. For the *OH intermediate, which corresponds to a fully hydroxylated surface, the top layer is exclusively Fe^{2+}, whereas the charge states of Fe for the *O and *OOH intermediates resemble more strongly the ones at *, except for the Fe^{4+} (magnetic moment 2.36 μ_B) at the reaction site for *O.

With Co incorporation, significant changes occur in the magnetic moments, signalling changes in valence and/or spin state. In contrast to bulk $LaCo_xFe_{1-x}O_3$ where Co^{3+} LS prevails, at LCFO(001) Co acquires a finite magnetic moment even in the third layer (0.68–2.90 μ_B). Unlike $x=0.000$, for $x=0.125$ the Fe reaction site is Fe^{2+} (*), changes to Fe^{3+} (*OH), Fe^{4+} for *O and back to Fe^{3+} for *OOH. Overall the presence of Co enhances the Fe^{3+} fraction in $LaCo_xFe_{1-x}O_3(001)$, albeit in the subsurface layer the Fe^{2+} fraction varies from 0 (*), to 1/4 (*OH and *O) and 1/2 (*OOH). For $x=0.250$ the charge states of the reaction site resemble rather those at $x=0.000$, whereas the variation of charge states at the Fe reaction site for $x=0.500$ are similar to the ones for $x=0.125$. This may explain the nonmonotonic trend in the overpotentials of the Fe reaction site with an initial decrease and subsequent increase of η both in the predicted and measured values at $x=0.250$. Interestingly, for $x=0.500$ Co in the third layer is low spin ($\sim 0.1\ \mu_B$), but the Co magnetic moment increases to $\sim 1.0-1.2\ \mu_B$ in the subsurface layer and to 2.2–2.97 μ_B in the surface layer which indicates a higher fraction of Co^{2+} at the surface.

Turning now to the Co reaction site in Figure 9, for $x=0.125$ its magnetic moment is reduced from initially $-2.13\ \mu_B$ (*) to $-1.26\ \mu_B$ (*OH and *O) and subsequently increased to $-1.58\ \mu_B$ (*OOH). For $x=0.250$ its magnetic moment is $-0.65\ \mu_B$ at * and increases to $-1.80\ \mu_B$ for the remaining intermediate steps. Finally, for $x=0.500$ the Co reaction site has a magnetic moment of 2.23 μ_B for all

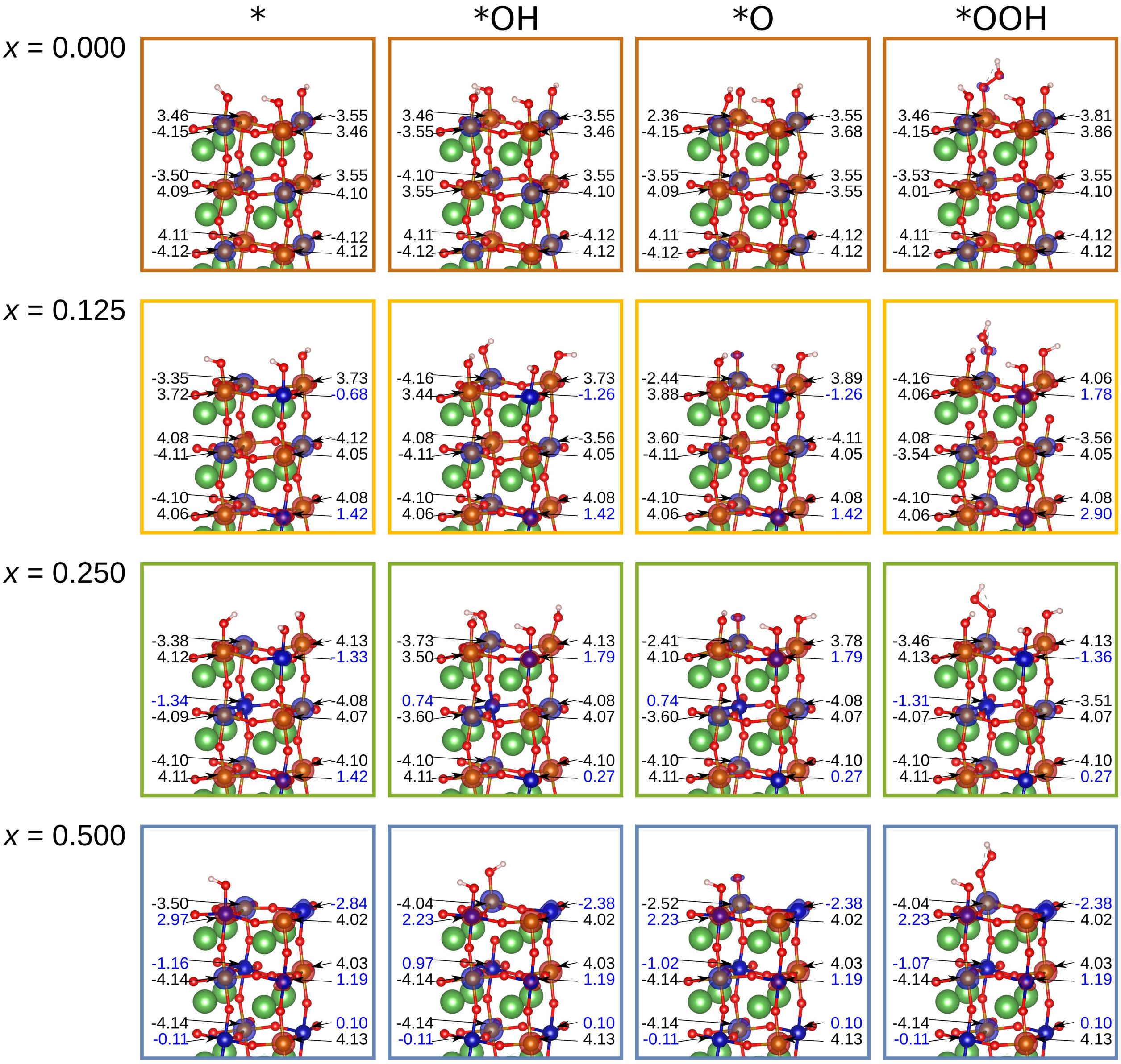

Figure 8. Side view of the relaxed structures together with the spin density of the hydroxylated surface for the four OER steps of a Fe reaction site at $LaCo_xFe_{1-x}O_3(001)$ with different concentrations x. Additionally, the magnetic moments of the Fe (black) and Co-cations (blue) in the three topmost layers are given in μ_B.

intermediates except for *OOH, where it is 1.15 μ_B. We note that due to the antiferromagnetic order of $LaCo_xFe_{1-x}O_3$, the active site has in some cases a positive and in some a negative magnetic moment. How the orientation of the magnetic moment may affect the OER activity is an important question that needs to be addressed in further studies.

While the magnetic moment of the Co reaction site shows less variation, more pronounced changes occur at the subsurface Co-sites with changes between 0.28 and 1.43 μ_B for $x = 0.125$ and 0.250. For $x = 0.500$, the magnetic moments of subsurface Co vary from 0.10 and 2.57 μ_B, whereas the third layer contains almost exclusively Co^{3+} LS. Fe^{2+} is present in the surface and, to a lesser extent, subsurface layer, but its fraction decreases noticeably with x, leading to an overall stabilization of Fe^{3+}.

Altogether, the fraction of bulk-like Fe^{3+} HS and Co^{3+} LS increases with x which may correlate with the nonmonotonic trend and subsequent increase of η. On the other hand, the substantial changes in magnetic moments at $LaCo_xFe_{1-x}O_3(001)$ during OER involve multiple ions also further away from the reaction site. In some cases the changes in magnetic moment are even more pronounced at the neighboring sites than at the reaction site, implying a concerted process with involvement of several coordination shells. This indicates that the concept of the active site goes significantly beyond the single reaction site and the surrounding cations, including deeper layers, play an important role and give important hints towards the synergy

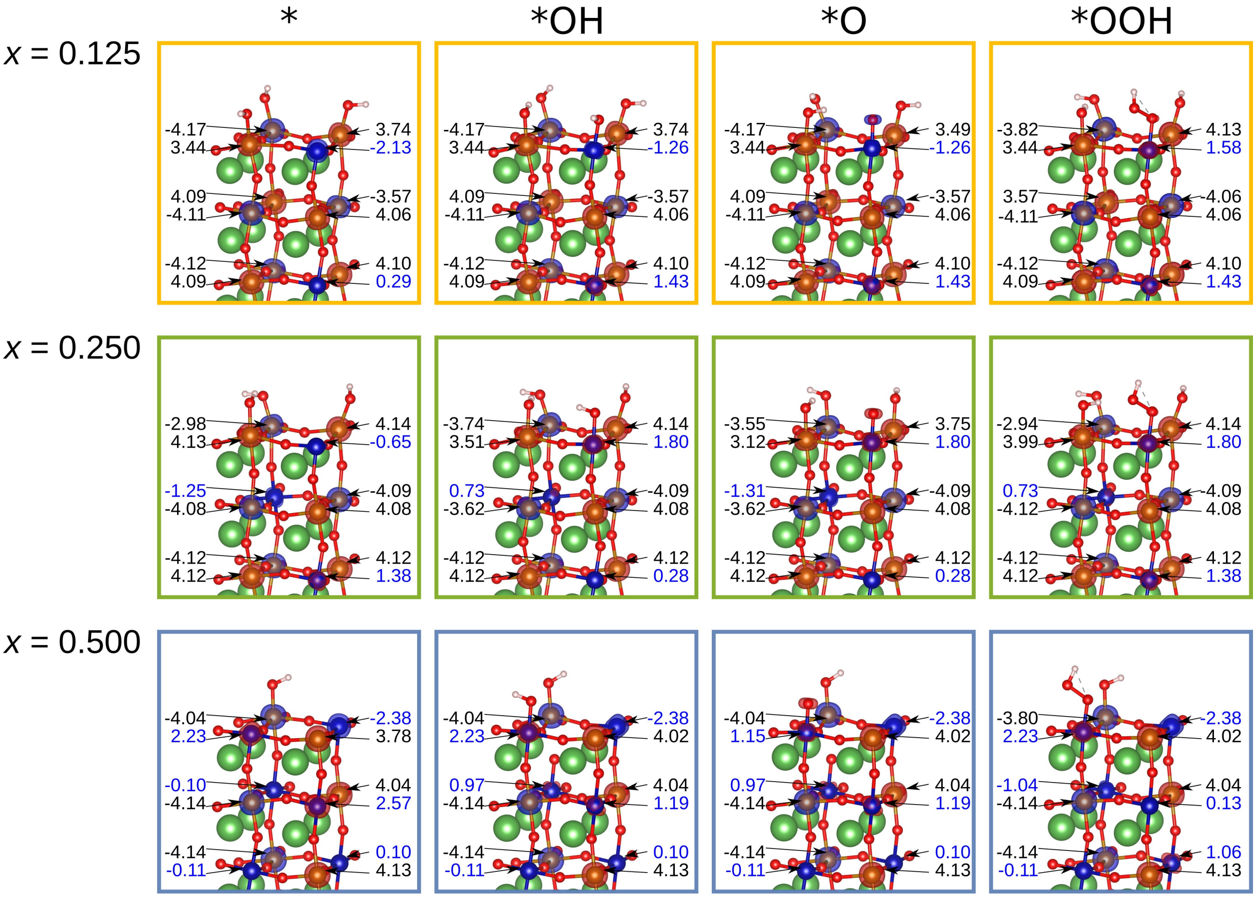

Figure 9. Side view of the relaxed structures together with the spin density of the hydroxylated surface for the four OER steps of a Co reaction site at $LaCo_xFe_{1-x}O_3(001)$ with different concentrations x. Additionally, the magnetic moments of the Fe (black) and Co-cations (blue) in the three topmost layers are given in μ_B.

effects between Co and Fe in LCFO as an anode material for OER.

3. Conclusions

In a combined experimental and theoretical study we explored the OER activity of $LaCo_xFe_{1-x}O_3$ as a function of Co concentration. Rotating disc electrode voltammetry of phase pure perovskites with a Co/(Co+Fe) ratio of up to 0.300, shows a substantial overpotential decrease of about 70 meV for even the smallest Co admixture of $x = 0.05$. Double layer capacitance measurements showing a slightly higher electrochemically active surface area for $LaFeO_3$ than for the Co-containing compounds suggest that the increase in OER-activity is intrinsic. The positive effect of Co incorporation and the nonmonotonic trend with x are confirmed by DFT+U calculations at BO_2-terminated $LaCo_xFe_{1-x}O_3(001)$ surfaces. This surface termination was found to be stable at the relevant synthesis conditions, according to the surface phase diagram and is also supported by TEM measurements. The calculations show that the OER overpotentials are reduced for both Fe and Co reaction sites with Co incorporation, but those of Co are significantly lower, reaching values of 0.32–0.40 V, compared to 0.60–0.67 V for Fe. This correlates with a lowering of the binding energy difference between $^*O$ and $^*OH$ to below 1.6 eV for Co at $x = 0.250$. We note that the deprotonation of $^*OH$ comprises the potential limiting step in the majority of cases considered. The nonmonotonic trend in the calculated microscopic overpotentials is correlated to the electronic and magnetic properties. We observe strong changes of the magnetic moments during OER, in particular with Co incorporation, indicative of changes in oxidation state, as found previously at spinel surfaces, e.g. $CoFe_2O_4$ and $Co_3O_4(001)$.[16,18] While a significant fraction of Fe^{2+} is present at the $LaFeO_3(001)$ surface and subsurface layer, Co enhances the fraction of Fe^{3+}, in particular in the deeper layers. Increase of the Co concentration reduces the variation in magnetic moments at the Co reaction site during OER, which seems to have a beneficial effect on the overpotential. In contrast to spinels where the neighboring sites are much less affected and the changes are concentrated at the reaction site,[16,18] for $LaCo_xFe_{1-x}O_3$ the changes in magnetic moments are by far not limited to the reaction site, but occur in several coordination shells up to the third layer. This may indicate a significant difference between perovskites and spinels. Moreover, it demonstrates that the surroundings of the reaction site plays an active role in the catalytic performance, pointing towards a generalization of the concept of the active site.

Experimental Methods

Raw Materials

For catalyst synthesis, commercially available reagents were used without further purification: iron(III) nitrate nonahydrate ($\geq$98%, Sigma-Aldrich GmbH, St. Louis, Missouri, USA), lanthanum(III) nitrate hexahydrate (99.9% La, abcr GmbH, Karlsruhe, Germany), cobalt(II) nitrate hexahydrate ($\geq$98%, Carl Roth GmbH, Karlsruhe, Germany), sodium carbonate ($\geq$99.5%, VWR International GmbH, Darmstadt, Germany), and sodium hydroxide (98.5%, Carl Roth GmbH, Karlsruhe, Germany).

Synthesis

The synthesis via co-precipitation was reported before,[42] and included the preparation of metal salt stock solutions with a total ionic concentration M^{n+} of 0.8 mol L^{-1} with the composition La^{3+}:Fe^{3+}:Co^{2+} $= 1:(1-x):x$ in deionized water. The value of x was varied in the range between 0 and 0.25. The precipitation agent consisted of 1.2 M NaOH and 0.18 M Na_2CO_3 in deionized water.

The syntheses were conducted in an automated synthesis workstation OptiMax 1001 (Mettler Toledo GmbH, Greifensee, Switzerland). The setup consisted of a single-walled glass reactor fixed inside a solid-state thermostat for accurate temperature control. During precipitation and aging steps, N_2 flow was employed, and the prefill volume of the reactor was purged with N_2 for 30 min. Co-precipitations were performed at a constant pH of 9.5 and an isothermal temperature of 10 °C. A precision balance controlled by a universal control box allowed gravimetric dosing of the metal salt solutions of 75 g in 36 min. Control over the pH was achieved by simultaneous computer-controlled dosing of the metal salt solution and the precipitation agent via two ProMinent gamma/L metering pumps. The pH was monitored and adjusted using an InLab Semi-Micro-L electrode before each experiment. A pitched blade impeller rotating at a constant speed of 300 rpm was used to avoid concentration and temperature gradients. After the precipitation was finished, an aging step at 10 °C for 60 min was performed. After aging, the precipitate was isolated by centrifugation (6000 rpm, 2 min) and washed with deionized water until the conductivity of the supernatant was below 0.1 mS cm^{-1} in two consecutive runs. Conductivity was measured using a Multi-Range Conductivity Meter HI 9033 (Hanna instruments, Graz, Austria), which was held in the supernatant in the middle of the centrifuge tube. Afterward, the samples were dried in static air at 80 °C for 12 h. The precursors were calcined at 800 °C for 3 h ($\beta = 2\,°\text{C min}^{-1}$) in stagnant air in a muffle furnace (B150, Nabertherm, Lilienthal, Germany). The calcined samples were characterized as powders.

Sample Characterization

Fe and Co contents in the precursors were determined by atomic absorption spectroscopy (M-Series, Thermo Electron Corporation, Waltham, Massachusetts, United States of America).

N_2 adsorption and desorption experiments were conducted after degassing the samples at 80 °C for 2 h in a vacuum with a NOVA3000e setup (Quantachrome Instruments, Boynton Beach, Florida, United States of America) at −196 °C. BET (Brunauer Emmet Teller) surface areas were calculated from p/p_0 data between 0.05 and 0.3. Total pore volumes were determined at $p/p_0 = 0.99$. Pore size distributions were determined using the BJH method during desorption.

Powder XRD patterns in the 2θ range from 5° to 90° were recorded on a Bruker D8 Advance (Bruker, Billerica, Massachusetts, USA) diffractometer in Bragg–Brentano geometry using a position-sensitive LYNXEYE detector (Ni-filtered CuK_α radiation, Bruker, Billerica, Massachusetts, USA) applying a counting time of 0.3 s and step size of 0.018°. Samples were mounted using dispersion in ethanol on a glass disc inserted in a round PMMA holder. The latter was subject to gentle rotation during scanning after removing the ethanol by drying.

High-resolution scanning transmission electron microscopy (STEM) studies were carried out on a Jeol JEM 2200 fs microscope (Akishima, Japan) equipped with a probe-side Cs-corrector operated at 200 kV acceleration voltage. Micrographs were taken in conventional bright field as well as in high-angle annular darkfield (HAADF) mode. In addition, EDX elemental mappings were acquired with an X–Max 100 detector (Oxford Instruments, Abingdon, United Kingdom).

Electrochemical Measurements

All electrochemical measurements were conducted with a three-electrode cell configuration setup using Metrohm Autolab PGSTAT potentiostat equipped with a rotator (Metrohm). A double-junction Ag/AgCl electrode (Metrohm) filled with 3 M KCl and 1 M KOH solution at the inner and outer compartments, respectively, was used as the reference electrode. A platinum mesh was used as the counter electrode, and was kept in a compartment separated by a glass frit during the measurements. A catalyst ink was prepared by dispersing 1 mg of catalyst powder in 200 μL of a solution comprising water, ethanol and Nafion solution (49:49:2 volume ratio). The working electrode was prepared by drop-casting 4.8 μL of catalyst ink over a glassy carbon rotating disk electrode of 0.1134 cm^2 geometric area to obtain a total catalyst loading of 210 $\mu\text{g/cm}^2$. Prior to drop-casting, the glassy carbon substrate was polished using 0.05 μm alumina paste until a mirror finishing was attained. Argon-saturated 1 M KOH was used as the electrolyte. The electrolyte was purified using a chelating ion resin (Chelex 100, Bio-Rad) to remove metal impurities. A stream of argon was flushed over the electrolyte during the measurements to maintain gas saturation.

Prior to activity tests, cyclic voltammetry was conducted in the potential window from −0.2 to 0.4 V vs Ag/AgCl/KCl at a scan rate of 0.1 V/s until reproducible voltammograms (CVs) were obtained. Subsequently, galvanostatic electrochemical impedance spectra-were recorded at 0 A in the frequency range from 100 kHz to 100 Hz with an AC amplitude of 10 μA (RMS). From the resulting Nyquist plots, the uncompensated resistance (R) was determined and was used to iR-drop-correct the measured potentials according to Eq. (1), considering the measured current (I).

$$E_{corrected} = E_{\text{measured}} - I \cdot R \tag{1}$$

To investigate the OER activity, linear sweep voltammetry (LSV) was conducted in the potential range from 0.1 to 0.8 V vs Ag/AgCl/KCl at a scan rate of 0.005 V/s and electrode rotation speed of 1600 rpm. All measurements were conducted in triplicate. The obtained currents were normalized with respect to the geometric area of the electrode. The measured potentials were converted to the reversible hydrogen electrode (RHE) scale using Eq. (2).

$$E_{\mathrm{RHE}} = E_{\mathrm{Ag/AgCl/KCl}} + 0.207 + 0.059 \cdot \mathrm{pH} \tag{2}$$

The pH of the KOH solution was calculated using Eq. (3), considering the activity of water (a_w) in KOH as reported in the literature.[60,61]

$$\mathrm{pH} = 14 + \log[\mathrm{OH}^-] + \log a_w \tag{3}$$

Double layer capacitance (C_{DL}) was determined for all perovskite samples following a procedure reported recently.[52] CVs were recorded in a potential window of about 0.4 V centered at the open circuit potential (OCP) at scan rates of 0.10, 0.25, 0.50, 0.75 and 1.00 V/s until reproducible voltammograms were obtained. OCP values and potential windows used for each of the samples are shown in Table S4. Charging currents measured at the potential corresponding to OCP ($_c$) were extracted from the anodic and cathodic sweeps of the last recorded CVs and plotted as a function of the scan rate (ν). The allometric regression model was used for determining C_{DL} according to Eq. (4).

$$I_C = C_{DL}\, \nu^{\alpha} \tag{4}$$

Computational Methods and Details

DFT calculations

The density functional theory calculations were carried out with the VASP code using pseudopotentials and the projector augmented wave (PAW) method.[62–65] The PBEsol exchange-correlation functional was used together with an effective Hubbard parameter $U_{\mathrm{eff}} = U - J$ within the Dudarev approach with $U_{\mathrm{eff}} = 4$ eV for Fe and 3.3 eV for Co,[66,67] obtained by fitting to bulk oxide formation enthalpies.[68,69] A plane wave cutoff of 520 eV and a $4 \times 4 \times 4$-Monkhorst-Pack *k*-point mesh were used for bulk $\mathrm{LaCo}_x\mathrm{Fe}_{1-x}\mathrm{O}_3$,[70] which was modelled using a $2 \times 2 \times 2$ pseudocubic unit cell to take into account different B-cation arrangements as well as octahedral tilts and distortions. The (001) oriented surfaces were modelled by slabs with a $2 \times 2 \times 13$ geometry and separated by 15.6 Å of vacuum in *z*-direction to avoid interaction between the slabs and the periodic images. For these a $4 \times 4 \times 1$ k-mesh was used. All systems were relaxed until the residual forces were below 0.01 eV/ Å. Since the adsorption was only modeled on one surface, a dipole-correction in the vertical direction was applied.

Surface stability and Pourbaix diagram

In the framework of *ab initio* thermodynamics,[57,58] the surface energy of a slab is given by:

$$\gamma = \frac{1}{2A}\left(E_* - M \cdot E_{bulk} - N_i \mu_i\right) \tag{5}$$

where E_* is the total energy of the slab with two surfaces with area A each, M the number the bulk units contained in the slab (3 in this case), E_{bulk} the bulk energy of the oxide, and N_i the number of excess ions of each species i (La, Co, Fe, O) in the slab and μ_i the corresponding chemical potentials. The chemical potentials are not independent but are related by the condition that the bulk oxide is stable, which defines the oxygen-poor conditions, beyond which the perovskite would decompose into binary oxides and, finally, into elemental compounds. These boundaries are determined by the formation enthalpies of the corresponding bulk materials. This allows to reduce the dimensionality of the surface phase diagram and plot it as a function of the chemical potentials of La and O for LaFeO_3 and additionally Fe for $\mathrm{LaCo}_x\mathrm{Fe}_{1-x}\mathrm{O}_3$. The oxygen-rich conditions are determined by the binding energy of a gas-phase oxygen molecule. Furthermore, the chemical potential of oxygen can be related to the synthesis conditions by converting it to temperature for a given oxygen partial pressure.

The Pourbaix diagram allows to determine the coverage of the surface with functional groups for given applied voltage U and pH.[59] The free energy of the surface covered by varying amounts of *O and *OH groups as a function of applied voltage U and pH is expressed by:

$$\begin{aligned}\Delta G = {} & E*_{+N_{\mathrm{O}}+N_{\mathrm{OH}}} - E* - \left(N_{\mathrm{O}} + N_{\mathrm{OH}}\right)\Delta H^f_{\mathrm{H_2O}} + \left(N_{\mathrm{O}} + \frac{1}{2}N_{\mathrm{OH}}\right)\Delta H^f_{\mathrm{H_2}} \\ & + \Delta ZPE - T\Delta S - \left(2N_{\mathrm{O}} + N_{\mathrm{OH}}\right)\left(eU + k_{\mathrm{B}}T \cdot \ln(10)\mathrm{pH}\right)\end{aligned} \tag{6}$$

$\left(E_{*+N_{\mathrm{O}}+N_{\mathrm{OH}}} - E_*\right)$ is the difference in total energy of the clean and covered slab, $N_{\mathrm{O,OH}}$ the number of *O and *OH adsorbates, $H^f_{H_2O}$ and $H^f_{H_2}$ the formation enthalpies of water and hydrogen, and ΔZPE is the change in zero point energy and $T \cdot \Delta S$ the entropy loss upon adsorption.

Modelling of OER

The overpotential was calculated following the approach of Nørskov and Rossmeisl.[71] Herein, the OER is divided into four coupled electron-proton transfer steps:

$$\text{Step 1}: \quad ^* + \mathrm{H_2O} \rightarrow {}^*\,\mathrm{OH} + \mathrm{H}^+ + \mathrm{e}^- \tag{7}$$

$$\text{Step 2}: \quad ^*\,\mathrm{OH} \rightarrow {}^*\,\mathrm{O} + \mathrm{H}^+ + \mathrm{e}^- \tag{8}$$

$$\text{Step 3}: \quad ^*\,\mathrm{O} + \mathrm{H_2O} \rightarrow {}^*\,\mathrm{OOH} + \mathrm{H}^+ + \mathrm{e}^- \tag{9}$$

$$\text{Step 4}: \quad ^*\,\mathrm{OOH} \rightarrow {}^* + \mathrm{O_2} + \mathrm{H}^+ + \mathrm{e}^- \tag{10}$$

where * denotes the pristine surface with the reaction site and *OH, *O and *OOH are the three reaction intermediates. The intermediates' binding energy ΔG^b_{ads} is given by:

$$\begin{aligned}\Delta G^b_{ads} = {} & E_* - E_{ads} + N_O \cdot H^f_{H_2O} - \left(N_O - \frac{1}{2}N_H\right) \\ & \cdot H^f_{H_2} + \Delta ZPE + T \cdot \Delta S - n_{ads}\, e\, \phi\end{aligned} \tag{11}$$

$E_* - E_{ads}$ is the total energy difference of the slab without and with adsorbate, N_{O} and N_{H} are the amounts of O and H atoms of the adsorbate, n_{ads} is the number of electron transfers taking place at the respective step, e the elementary charge and ϕ is the applied potential. Previous studies have shown that ΔZPE and $T \cdot \Delta S$ do not change significantly at different transition metal oxide surfaces,[72] thus we adopted the values reported in this work. Under electrochemical standard conditions and in relation to the standard hydrogen electrode (SHE), the steps between these intermediates are given by:

$$\Delta G_i = \Delta G^b_{ads_2} - \Delta G^b_{ads_1} + k_B T \cdot \ln(10)\ \mathrm{pH} \tag{12}$$

where $\Delta G^b_{ads_{1,2}}$ are two consecutive intermediates' adsorption energies. The minimal external potential ϕ that makes all ΔG_i negative, and thus the whole reaction energetically downhill is thus given by the potential-determining step:

$$\phi_{\mathrm{OER}} = \max[\Delta G_i]/e \tag{13}$$

The overpotential is accordingly calculated as:

$$\eta = \phi_{\mathrm{OER}} - 1.23\ \mathrm{V} \tag{14}$$

Acknowledgement

We acknowledge gratefully funding by the Deutsche Forschungsgemeinschaft (DFG, German Research Foundation) – 388390466 – TRR 247 within projects A1, A2, B4 and C1, as well as the Mercator Research Center Ruhr (MERCUR, Pe-2018-0034). The authors thank Robin Meya and Beate Römer for providing AAS measurements and Dietrich Tönnes for the XRD measurements. The authors also acknowledge Dr. Markus Heidelmann for TEM measurements. Furthermore, we acknowledge computational time at SuperMUC at the Leibniz Rechenzentrum (project pr87ro) and at MagnitUDE at UDE (DFG grant INST 20876/209-1 FUGG) and support by the Open Access Publication Fund of the University of Duisburg-Essen. Open Access funding enabled and organized by Projekt DEAL.

Conflict of Interest

The authors declare no conflict of interest.

[1] W. T. Hong, M. Risch, K. A. Stoerzinger, A. Grimaud, J. Suntivich, Y. Shao-Horn, *Energy Environ. Sci.* **2015**, *8*, 1404–1427.
[2] Y. Cheng, S. P. Jiang, *Prog. Nat. Sci.* **2015**, *25*, 545–553.
[3] S. Kalantarifard, S. I. Allakhverdiev, M. M. Najafpour, *Int. J. Hydrogen Energy* **2020**, *45*, 33563–33573.
[4] L. Zhang, Q. Fan, K. Li, S. Zhang, X. Ma, *Sustain. Energy Fuels* **2020**, *4*, 5417–5432.
[5] J. Suntivich, K. J. May, H. A. Gasteiger, J. B. Goodenough, Y. Shao-Horn, *Science* **2011**, *334*, 1383–1385.
[6] A. Dutta, S. Mutyala, A. K. Samantara, S. Bera, B. K. Jena, N. Pradhan, *ACS Energy Lett.* **2017**, *3*, 141–148.
[7] C. Xiao, X. Lu, C. Zhao, *Chem. Commun.* **2014**, *50*, 10122–10125.
[8] O. Diaz-Morales, I. Ledezma-Yanez, M. T. Koper, F. Calle-Vallejo, *ACS Catal.* **2015**, *5*, 5380–5387.
[9] D. A. Corrigan, *J. Electrochem. Soc.* **1987**, *134*, 377.
[10] J. Xu, J. Li, D. Xiong, B. Zhang, Y. Liu, K.-H. Wu, I. Amorim, W. Li, L. Liu, *Chem. Sci.* **2018**, *9*, 3470–3476.
[11] H. Jin, S. Mao, G. Zhan, F. Xu, X. Bao, Y. Wang, *J. Mater. Chem. A* **2017**, *5*, 1078–1084.
[12] M. S. Burke, M. G. Kast, L. Trotochaud, A. M. Smith, S. W. Boettcher, *J. Am. Chem. Soc.* **2015**, *137*, 3638–3648.
[13] D. Guo, H. Kang, P. Wei, Y. Yang, Z. Hao, Q. Zhang, L. A. Liu, *CrystEngComm* **2020**, *22*, 4317–4323.
[14] K. Chakrapani, G. Bendt, H. Hajiyani, I. Schwarzrock, T. Lunkenbein, S. Salamon, J. Landers, H. Wende, R. Schlögl, R. Pentcheva, M. Behrens, S. Schulz, *ChemCatChem* **2017**, *9*, 2988–2995.
[15] K. Chakrapani, G. Bendt, H. Hajiyani, T. Lunkenbein, M. T. Greiner, L. Masliuk, S. Salamon, J. Landers, R. Schlögl, H. Wende, R. Pentcheva, S. Schulz, M. Behrens, *ACS Catal.* **2018**, *8*, 1259–1267.
[16] H. Hajiyani, R. Pentcheva, *ACS Catal.* **2018**, *8*, 11773–11782.
[17] E. Budiyanto, M. Yu, M. Chen, S. DeBeer, O. Rüdiger, H. Tüysüz, *ACS Appl. Energ. Mater.* **2020**.
[18] Y. Peng, H. Hajiyani, R. Pentcheva, *ACS Catal.* **2021**, *11*, 5601–5613.
[19] J. Han, G. Chen, X. Liu, N. Zhang, S. Liang, R. Ma, G. Qiu, *Chem. Commun. (Camb.)* **2019**, *55*, 9212–9215.
[20] Y. Li, X. Jiang, M. Tang, Q. Zheng, Y. Huo, F. Xie, D. Lin, *Int. J. Hydrogen Energy* **2020**, *45*, 28586–28597.
[21] S. Klemenz, J. Schuch, S. Hawel, A.-M. Zieschang, B. Kaiser, W. Jaegermann, B. Albert, *ChemSusChem* **2018**, *11*, 3150–3156.
[22] D. Li, Y. Xing, R. Yang, T. Wen, D. Jiang, W. Shi, S. Yuan, *ACS Appl. Mater. Interfaces* **2020**, *12*, 29253–29263.
[23] Y. Wang, D. Liu, Z. Liu, C. Xie, *Chem. Commun. (Camb.)* **2016**, *52*, 12614–12617.
[24] L. Wu, D. Shi, S. Yan, W. Qiao, W. Zhong, Y. Du, *Int. J. Hydrogen Energy* **2021**, *46*, 2086–2094.
[25] S. Royer, D. Duprez, F. Can, X. Courtois, C. Batiot-Dupeyrat, S. Laassiri, H. Alamdari, *Chem. Rev.* **2014**, *114*, 10292–10368.
[26] J. Hwang, R. R. Rao, L. Giordano, Y. Katayama, Y. Yu, Y. Shao-Horn, *Science* **2017**, *358*, 751–756.
[27] D. Antipin, M. Risch, *J. Phys. Energy* **2020**, *2*, 032003.
[28] M. H. Seo, H. W. Park, D. U. Lee, M. G. Park, Z. Chen, *ACS Catal.* **2015**, *5*, 4337–4344.
[29] A. Vojvodic, J. K. Nørskov, *Science* **2011**, *334*, 1355–1356.
[30] J. T. Mefford, X. Rong, A. M. Abakumov, W. G. Hardin, S. Dai, A. M. Kolpak, K. P. Johnston, K. J. Stevenson, *Nat. Commun.* **2016**, *7*, 1–11.
[31] A. Grimaud, O. Diaz-Morales, B. Han, W. T. Hong, Y.-L. Lee, L. Giordano, K. A. Stoerzinger, M. T. Koper, Y. Shao-Horn, *Nat. Chem.* **2017**, *9*, 457–465.
[32] J. S. Yoo, X. Rong, Y. Liu, A. M. Kolpak, *ACS Catal.* **2018**, *8*, 4628–4636.
[33] Y. Zhu, W. Zhou, J. Yu, Y. Chen, M. Liu, Z. Shao, *Chem. Mater.* **2016**, *28*, 1691–1697.
[34] Y. Duan, S. Sun, S. Xi, X. Ren, Y. Zhou, G. Zhang, H. Yang, Y. Du, Z. Xu, *Chem. Mater.* **2017**, *29*, 10534–10541.
[35] I. C. Man, H.-Y. Su, F. Calle-Vallejo, H. A. Hansen, J. I. Martinez, N. G. Inoglu, J. Kitchin, T. F. Jaramillo, J. K. Nørskov, J. Rossmeisl, *ChemCatChem* **2011**, *3*, 1159–1165.
[36] Y.-L. Lee, M. J. Gadre, Y. Shao-Horn, D. Morgan, *Phys. Chem. Chem. Phys.* **2015**, *17*, 21643–21663.
[37] X. Rong, J. Parolin, A. M. Kolpak, *ACS Catal.* **2016**, *6*, 1153–1158.
[38] V. Tripkovic, H. A. Hansen, J. M. Garcia-Lastra, T. Vegge, *J. Phys. Chem. C* **2018**, *122*, 1135–1147.
[39] K. Zhao, F. He, Z. Huang, G. Wei, A. Zheng, H. Li, Z. Zhao, *Appl. Energy* **2016**, *168*, 193–203.
[40] L. Bedel, A. Roger, C. Estournes, A. Kiennemann, *Catal. Today* **2003**, *85*, 207–218.
[41] J. Xu, J. Liu, Z. Zhao, J. Zheng, G. Zhang, A. Duan, G. Jiang, *Catal. Today* **2010**, *153*, 136–142.
[42] M. Dreyer, M. Krebs, S. Najafishirtari, A. Rabe, K. Friedel Ortega, M. Behrens, *Catalysts* **2021**, *11*, 550.
[43] R. Allmann, H. P. Jepsen, *Neues Jahrb. Mineral. Monatsh.* **1969**, *12*, 544 A' 551.
[44] L. Sangaletti, L. E. Depero, B. Allieri, P. Nunziante, E. Traversa, *J. Eur. Ceram. Soc.* **2001**, *21*, 719–726.
[45] R. D. Shannon, *Acta Crystallogr. Sect. A* **1976**, *32*, 751–767.
[46] V. M. Gaikwad, S. A. Acharya, *RSC Adv.* **2015**, *5*, 14366–14373.
[47] H. Cui, M. Zayat, D. Levy, *J. Non-Cryst. Solids* **2006**, *352*, 3035–3040.
[48] M. Thommes, K. Kaneko, A. V. Neimark, J. P. Olivier, F. Rodriguez-Reinoso, J. Rouquerol, K. S. Sing, *Pure Appl. Chem.* **2015**, *87*, 1051–1069.
[49] K. Elumeeva, M. A. Kazakova, D. M. Morales, D. Medina, A. Selyutin, G. Golubtsov, Y. Ivanov, V. Kuznetzov, A. Chuvilin, H. Antoni, *ChemSusChem* **2018**, *11*, 1204–1214.
[50] S. He, H. Lin, *Nanoscale* **2019**, *11*, 10348–10357.
[51] L. Trotochaud, S. L. Young, J. K. Ranney, S. W. Boettcher, *J. Am. Chem. Soc.* **2014**, *136*, 6744–6753.
[52] D. M. Morales, M. Risch, *J. Phys. Energy* **2021**, *3*, 034013.
[53] A. M. Ritzmann, M. Pavone, A. B. Muñoz-García, J. A. Keith, E. A. Carter, *J. Mater. Chem. A* **2014**, *2*, 8060–8074.
[54] J. Buckeridge, F. Taylor, C. Catlow, *Phys. Rev. B* **2016**, *93*, 155123.
[55] H. Hsu, P. Blaha, R. M. Wentzcovitch, C. Leighton, *Phys. Rev. B* **2010**, *82*, 100406.
[56] B. Geisler, R. Pentcheva, *Phys. Rev. B* **2020**, *101*, 165108.
[57] K. Reuter, M. Scheffl, *Phys. Rev. B* **2001**, *65*, 035406.
[58] K. Krishnaswamy, C. Dreyer, A. Janotti, C. Van de Walle, *Phys. Rev. B* **2014**, *90*, 235436.
[59] H.-Y. Su, Y. Gorlin, I. C. Man, F. Calle-Vallejo, J. K. Nørskov, T. F. Jaramillo, J. Rossmeisl, *Phys. Chem. Chem. Phys.* **2012**, *14*, 14010–14022.
[60] M. Knobel, *J. Am. Chem. Soc.* **1923**, *45*, 70–76.
[61] L. A. Bromley, *AIChE J.* **1973**, *19*, 313–320.
[62] G. Kresse, J. Hafner, *Phys. Rev. B* **1993**, *47*, 558.
[63] G. Kresse, J. Furthmüller, *Comput. Mater. Sci.* **1996**, *6*, 15–50.
[64] G. Kresse, J. Furthmüller, *Phys. Rev. B* **1996**, *54*, 11169.
[65] P. E. Blöchl, *Phys. Rev. B* **1994**, *50*, 17953.

[66] S. Dudarev, G. Botton, S. Savrasov, C. Humphreys, A. Sutton, *Phys. Rev. B* **1998**, *57*, 1505.
[67] G. I. Csonka, J. P. Perdew, A. Ruzsinszky, P. H. Philipsen, S. Lebègue, J. Paier, O. A. Vydrov, J. G. Ángyán, *Phys. Rev. B* **2009**, *79*, 155107.
[68] L. Wang, T. Maxisch, G. Ceder, *Phys. Rev. B* **2006**, *73*, 195107.
[69] Y.-L. Lee, J. Kleis, J. Rossmeisl, D. Morgan, *Phys. Rev. B* **2009**, *80*, 224101.
[70] H. J. Monkhorst, J. D. Pack, *Phys. Rev. B* **1976**, *13*, 5188.
[71] J. Rossmeisl, Z.-W. Qu, H. Zhu, G.-J. Kroes, J. K. Nørskov, *J. Electroanal. Chem.* **2007**, *607*, 83–89.
[72] P. Liao, J. A. Keith, E. A. Carter, *J. Am. Chem. Soc.* **2012**, *134*, 13296–13309.

Manuscript received: August 3, 2021
Accepted manuscript online: September 8, 2021
Version of record online: October 27, 2021